Metals & corrosion

Refractory high-entropy nanoalloys with exceptional high-temperature stability and enhanced sinterability

Mingde Qin[1], Sashank Shivakumar[1], and Jian Luo[1,*]

[1] *Department of NanoEngineering, Program of Materials Science and Engineering, University of California San Diego, La Jolla, CA 92093, USA*

ABSTRACT

Nanocrystalline alloys (nanoalloys) are prone to grain growth. It is known that grain boundary segregation and precipitation can stabilize nanoalloys, but the stabilization becomes less effective at high temperatures and adding grain growth inhibitors often reduces sinterability. Herein, we have simultaneously achieved exceptional high-temperature stability and improved sinterability for a class of TiNbMoTaW-based refractory high-entropy nanoalloys (RHENs). Bulk pellets of RHENs were fabricated through ball milling and spark plasma sintering, achieving 93–96% relative densities with 50–100 nm grain sizes for three compositions. For example, $Ti_{17.8}Nb_{17.8}Mo_{17.8}Ta_{17.8}W_{17.8}Ni_6Zr_5$ sintered at 1300 °C attained $\sim$ 96% relative density with $\sim$ 55 nm mean grain size. Moreover, these RHENs exhibited exceptional stability at 1300 °C. Both $Ti_{17.8}Nb_{17.8}Mo_{17.8}Ta_{17.8}W_{17.8}Ni_6Zr_5$ and $Ti_{18.8}Nb_{18.8}Mo_{18.8}Ta_{18.8}W_{18.8}Ni_6$ retained < 150 nm grain sizes after five hours annealing at 1300 °C. Notably, the addition of Ni, a well-known sintering aid for activated sintering of refractory metals such as W and Mo, in high-entropy TiNbMoTaW can promote sintering while maintaining high-temperature stability against rapid grain growth. This may be explained by hypothesized high-entropy grain boundary (HEGB) effects, while we recognize the possible (additional) effects of compositional inhomogeneity and secondary phase (Zener) pinning. These RHENs possess some of the highest temperature stability achieved for nanoalloys and ultrafine-grained metals.

Introduction

Nanocrystalline metals show great potential as structural materials through improvements in strength, hardness, and wear resistance that stem from a reduction in grain size [1–6]. However, their applications are limited due to poor thermal stability [4–6]. Specifically, a large amount of grain boundaries (GBs) lead to a considerable increase in the total interfacial (GB) energy, thereby causing rapid and uncontrolled grain growth—in some cases, even at room temperature [4–7]. The stabilization of nanocrystalline alloys (nanoalloys) is commonly achieved through kinetic (impurity solute-drag effects [8] and/or secondary particle Zener pinning [9]) and/or thermodynamic (segregation induced GB energy reduction [10–18]) effects. Using these strategies, stable binary and ternary nanoalloys have been reported [4, 5, 10–18]. However, both thermodynamic and kinetic stabilization mechanisms are significantly weakened at high temperatures due to thermally induced GB desorption (de-segregation), coarsening of pinning particles, and increased GB mobilities, resulting in loss of desirable properties [4, 5, 19–22]. Nanocrystalline high-entropy alloys (HEAs) have also been made, which appear to exhibit enhanced stability against grain growth in comparison with their lower-entropy counterparts [23–25]. In 2016, Zhou et al. introduced the concept of high-entropy grain boundaries (HEGBs) [26, 27] and experimentally demonstrated the stabilization of nanoalloys at elevated temperatures using HEGBs [27]. The theory of HEGBs has been further elaborated recently in a Perspective article [28]. Of particular interest to this study is the so-called "Type II HEGBs" (*i.e.*, HEGBs in HEAs with one primary high-entropy phase and multiple secondary phases), where bulk high-entropy effects can be used to stabilize (multi-phase) nanocrystalline HEAs with one strong segregating element at high temperatures [27, 28]. Specifically, it was conjectured [27, 28] that adding a small amount of one segregating element in HEA grains can provide improved high-temperature stability against grain growth (in comparison with lower-entropy alloys) via both thermodynamic and kinetic effects, a hypothesis that motivated this study.

Furthermore, adding grain growth inhibitors can often reduce sinterability (if the nanoalloys are fabricated via powder metallurgy routes). Here, it is also well known that certain sintering aids can be used to enhance sintering [29–31] (in particular, to promote solid-state activated sintering via the formation of liquid-like GBs with high mass transport rates as one possible mechanism, as shown in Ni-activated sintering of W [32] and Mo [33] as two binary model systems, supported by a series of microscopy [34, 35] and thermodynamic modeling [33, 36, 37] studies), which can also promote grain growth because of the enhanced GB kinetics. Here, suppressing grain growth via reducing GB motion and enhancing sintering via increasing GB diffusion often represent two contradictory requirements. In this study, we found, somewhat surprisingly, that the addition of Ni, a well-known sintering aid for enabling solid-state activated sintering of W and Mo [31–33, 38, 39], in high-entropy TiNbMoTaW nanoalloys can promote sintering without accelerating grain growth, which can be explained from the hypothesized HEGB effects.

Motivated by prior studies of activated sintering [29, 31, 39] (especially promoting densification via segregation-enhanced GB diffusion [29, 32, 33]) and the hypothesized theory of Type II HEGBs (*i.e.*, adding a segregating element in nanocrystalline HEAs to inhibit grain growth at high temperatures [27, 28]), we added Ni (a well-known sintering aid for W and Mo via forming liquid-like GBs [29, 32, 33]) and/or Zr (a more refractory segregant in refractory metals) in TiNbMoTaW HEAs to test their effects on sintering and grain growth. Notably, we have demonstrated simultaneous improvements in sinterability and high-temperature stability against rapid grain growth to attain high relative densities of 93–96% and small mean grain sizes of 50–100 nm for (multiphase) refractory high-entropy nanoalloys (RHENs). For example, $Ti_{17.8}Nb_{17.8}Mo_{17.8}Ta_{17.8}W_{17.8}Ni_6Zr_5$ achieved ∼ 96% relative density with an as-sintered mean grain size of ∼ 55 nm, while simultaneously retaining < 150 nm grain sizes after annealing at 1300 °C for 5 h.

Materials and methods

RHENs were synthesized by mixing elemental powders of Mo, Nb, Ta, Ti, W, Ni, and Zr (> 99.5% purity, 325 mesh, Alfa Aesar, MA, USA). For each composition, appropriate amounts of powders were weighed out in batches of 20 g and planetary ball

milled (using a mill from Across International, NJ, USA) for 24 h at 300 RPM. Isopropyl alcohol (IPA) was used as a processing agent, and polytetrafluoroethylene (PTFE) vials and Y_2O_3-stablized ZrO_2 (YSZ) grinding media (at a ball-to-powder ratio of 10:1) were used for the milling process. After milling, the vials were transferred into a vacuum furnace and dried overnight at 75 °C to remove the processing agent, and then immediately transferred into a low oxygen environment (Ar glovebox, < 15 ppm O_2) to prevent oxidation of the fine powders. The powders were then loaded into 10 mm graphite dies (Cal Nano, CA, USA) lined with graphite and Mo foils in batches of 3 g and subsequently consolidated into dense pellets via spark plasma sintering (SPS) in vacuum (10^{-3}–10^{-2} torr) using a Thermal Technologies 3000 series SPS machine. A ramp rate of 100 °C/min was utilized and a hold time of 5 min was employed under 50 MPa of pressure at isothermal sintering temperatures. Samples were furnace cooled under vacuum. In total, specimens of 24 different compositions and SPS conditions were sintered, which are listed in Supplementary Table S1.

Isothermal annealing was performed on seven series of specimens at 1100 °C, 1200 °C, and 1300 °C, respectively, for 5 h in a tube furnace under flowing Ar + 5% H_2. In total, 21 specimens of seven compositions were annealed at three different temperatures, which are listed in Supplementary Table S2, along with the seven as-sintered specimens as references.

After sintering, bulk specimens were ground to remove Mo foils as well as the carbon-contaminated surface layers caused by the graphite tooling. XRD was performed on a Rigaku Miniflex diffractometer (Cu Kα radiation, 30 kV and 15 mA). Density measurements were taken using the Archimedes method. Theoretical densities were calculated from ideal stoichiometry and the lattice parameters measured by X-ray diffraction (XRD). Rockwell hardness (HRC) measurements were taken using a Wilson 574 series Rockwell tester (Buehler, IL, USA) equipped with a diamond spheroconical indenter abiding by the ASTM standard E18-15 with over 30 measurements to ensure the validity.

Samples were fractured after embrittling in liquid N_2 and scanning electron microscopy (SEM) was subsequently performed using a Thermo-Fisher Apreo microscope to examine the fractured surfaces. The grain size distributions were obtained from the corresponding SEM images following the ASTM standard E112-88.

Results and discussion

Design of compositions and overview of sintering and grain growth experiments

TiNbMoTaW or $Ti_{0.2}Nb_{0.2}Mo_{0.2}Ta_{0.2}W_{0.2}$ is our baseline composition that is denoted as "RHEN-0". This composition was then doped with 6% Ni ($Ti_{18.8}Nb_{18.8}Mo_{18.8}Ta_{18.8}W_{18.8}Ni_6$, denoted as "RHEN-6Ni") and 5% Zr ($Ti_{19}Nb_{19}Mo_{19}Ta_{19}W_{19}Zr_5$, denoted as "RHEN-5Zr"). Furthermore, we tested two co-doped compositions, $Ti_{17.8}Nb_{17.8}Mo_{17.8}Ta_{17.8}W_{17.8}Ni_6Zr_5$ (denoted as "RHEN-6Ni-5Zr") and $Ti_{18.9}Nb_{18.9}Mo_{18.9}Ta_{18.9}W_{18.9}Ni_3Zr_{2.5}$ (denoted as "RHEN-3Ni-2.5Zr").

Specimens of these five different compositions were sintered by SPS at different temperatures (at 1200 °C, 1300 °C, 1400 °C, and 1500 °C, respectively, for all five compositions and at 1100 °C, 1600 °C, and 1700 °C for selected compositions). For example, RHEN-6Ni sintered at 1300 °C by SPS is denoted as "RHEN-6Ni-1300SPS". The sintered bulk specimens were all pellets with a fixed diameter of 10 mm and thicknesses of ~ 3 mm. Measured relative density and grain size vs. SPS temperature curves for all five series of sintered specimens are shown in Fig. 1. Both relative density and grain size of each composition increased with SPS temperature (Fig. 1), which is well expected. Figure 2 further plots grain size vs. relative density curves for five series of specimens after SPS, where the mean grain size generally increased with increasing relative density, following similar trends (but with shifts in the curve positions). In comparison with RHEN-0, Ni-doping and (Ni + Zr) co-doping shifted the grain size vs. relative density curves towards the right (i.e., higher density with smaller grain sizes, which is desirable), while Zr-doping shifted the curve towards the left (undesirable).

The sintered specimens consisted primarily of body-centered cubic (BCC) phases, with (expected) secondary phases. For example, XRD patterns for RHEN-6Ni and RHEN-6Ni-5Zr synthesized at 1300 °C showed primary BCC phases (Supplementary Fig. S1); however, minor peak splitting suggested some compositional inhomogeneity after SPS

(not surprising given the short SPS time of only 5 min) and additional low-intensity peaks corresponding to minor secondary phases were also observed. The presence of minor secondary phases was well expected since we doped Ni and Zr beyond their solid solubility limits (Table 3) and some native oxides and other impurities (including possible contaminants) inevitably existed and could also form during ball milling. Note that we specifically designed our doping levels to above the five X-Ni and two X-Zr binary solubility limits, and therefore expect multiple secondary precipitation phases (e.g., equilibrium binary Mo_7Ni_7, Ta_2Ni, Nb_7Ni_6, W_2Zr, and Mo_2Zr compounds as based on the binary phase diagrams shown in Supplementary Figs. S2-S3, as well as ternary and multicomponent compounds at 1300 °C, along with additional precipitates during cooling) to be present, which are difficult to fully identify due to the large number (up to five or more based on the Gibbs phase rule) of the secondary phases and the small amounts of each phase. We also recognize the possible existence of compositional inhomogeneity in as-sintered RHENs, given the relatively low SPS temperatures (in comparison with the melting temperatures of refractory metals and alloys; e.g., 1300 °C is only ∼ 54% of the average melting temperatures of W, Mo, Nb, Ta, and Ti) and short sintering durations (5 min). Supplementary Fig. S4 further shows XRD patterns of three selected specimens, RHEN-0, RHEN-5Zr, and RHEN-5Zr-6Ni, after annealing at 1300 °C for 5 h. In all cases, the primary phase was identified to be the BCC phase. As expected, multiple secondary phase peaks are also observable for annealed specimens.

Up to five or six precipitate phases were anticipated based on the Gibbs phase rule and our compositional designs. In this regard, all Ni- and/or Zr-doped RHENs are multiphase with a primary BCC phase and several secondary phases (as designed). Such secondary phases can provide some Zener pinning. In addition, we expect some compositionally inhomogeneity in these RHENs, which can be more significant in as-sintered specimens.

Supplementary Fig. S5 shows SEM micrographs of fractured surfaces in selected as sintered and post-annealed compositions (RHEN-6Ni-1300SPS, RHEN-6Ni-1400SPS, RHEN-6Ni-5Zr-1300SPS). Supplementary Fig. S6 shows polished section SEM micrographs of selected post-annealed compositions (RHEN-0-1600SPS, RHEN-6Ni-1400SPS, RHEN-5Zr-1600SPS, RHEN-6Ni-5Zr-1600SPS).

Selected as-sintered RHENs that achieved 93–96% relative densities with 50–100 nm grain sizes are listed in Table 1. Notably, RHEN-6Ni-5Zr-1300SPS ($Ti_{17.8}Nb_{17.8}Mo_{17.8}Ta_{17.8}W_{17.8}Ni_6Zr_5$, SPS at 1300 °C) attained ∼ 96% relative density with ∼ 55 nm grain size. Results of all 24 as-sintered specimens made in this study are documented in Supplementary Table S1. These sintering results, particularly the effects of adding Ni and/or Zr, will be further discussed in the subsequent sections.

Grain growth experiments were performed on seven series of selected as-sintered RHENs by annealing them isothermally at 1100 °C, 1200 °C, and 1300 °C, respectively, for 5 h. Table S2 documents a detailed account of SPS temperature, annealing conditions, densities, and measured grain sizes of all 21 annealed specimens, along with seven as-sintered specimens before annealing as references. Figure 3a and b plot the changes in relative density and grain size with annealing temperature. All as-sintered compositions achieved relative densities > 85%, with grain sizes < 100 nm, except the base RHEN-0-1600SPS which exhibited the largest as-sintered grain size of ∼ 105 nm. Grain size and relative densities increased with annealing temperatures as expected, and all compositions retained average grain sizes < 150 nm even after 5 h of annealing at 1300 °C. These grain growth results will also be further discussed in the subsequent sections.

We also measured Rockwell hardness for three selected RHENs (RHEN-6Ni-1300SPS, RHEN-6Ni-1400SPS, and RHEN-6Ni-5Ni-1300SPS) after annealing at 1300 °C for 5 h, all of which exhibited similar (96.3–97.2%) relative densities and (124–133 nm) grain sizes (Table 2). The measured hardness values were 64 ± 3 HRC (RHEN-6Ni-1300SPS), 65 ± 2 HRC (RHEN-6Ni-1400SPS), and 62 ± 4 HRC (RHEN-6Ni-5Zr-1300SPS), respectively, as shown in Table 2.

The benchmark RHEN-0 ($Ti_{0.2}Nb_{0.2}Mo_{0.2}Ta_{0.2}W_{0.2}$) Specimens

The benchmark RHEN-0 ($Ti_{0.2}Nb_{0.2}Mo_{0.2}Ta_{0.2}W_{0.2}$) specimens generally showed limited sinterability with small grain sizes. The relative density of as-sintered RHEN-0 increased from ∼ 72.1% (with a small mean grain size of ∼ 11 nm) at a low SPS temperature of 1200 °C to 90.7% (with the mean grain

size being increased by almost tenfold to ~ 105 nm) at a high SPS temperature of 1600 °C (Fig. 1 and Supplementary Table S1). We further annealed the densest RHEN-0-1600SPS (SPS at 1600 °C) isothermally at 1100 °C, 1200 °C, and 1300 °C, respectively, for 5 h, which resulted in limited further densification and grain growth (Fig. 2 and Supplementary Table S2). For example, annealing at 1300 °C for 5 h increased the relative density of RHEN-0 moderately from $\sim 90.7\%$ to $\sim 91.2\%$, with a moderate increase of the mean grain size from ~ 105 nm to ~ 127 nm.

The effects of Zr *vs.* Ni doping

Here, we selected Ni and Zr as two doping (alloying) elements, both of which segregate at GBs of X = Mo, Nb, Ta, Ti, or W in all ten X-Ni and X-Zr binary alloys (Table 3). The binary segregation enthalpies estimated using a Miedema-based model by Murdoch and Schuh [40] range from $-24{,}897$ J/mol for Ti-Ni to $-78{,}276$ J/mol for W–Ni, with a rule-of-mixture (RoM) average of $-54{,}486$ J/mol for the five X-Ni alloys, and range from $-1{,}280$ J/mol for Ti-Zr to $-58{,}933$ J/mol for W-Zr, with a RoM average of $-31{,}552$ J/mol for the five X-Zr alloys (Table 3). Except for Ti-Zr, all other nine binary alloys can be considered as strong segregation systems. Here, it should be noted that we adopt a sign convention where a negative ΔH_{seg} value suggests GB enrichment or positive segregation [41] (differing from the
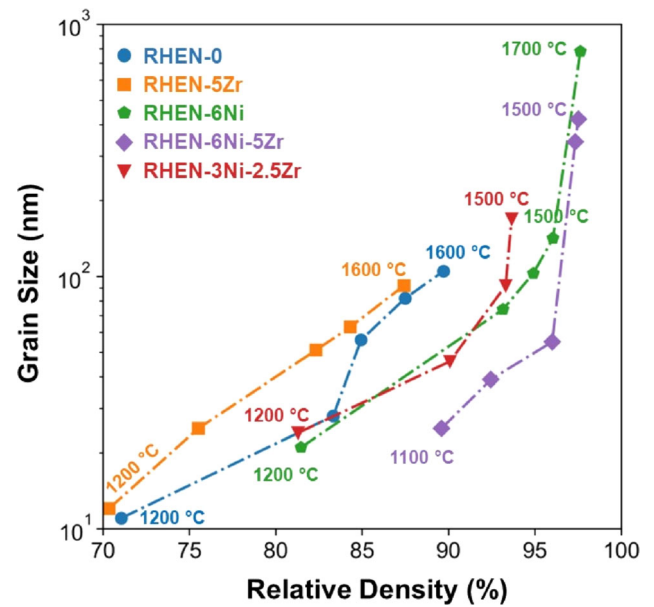

Figure 2 Grain size *vs.* relative density curves for five series of RHENs after SPS.

sign convention used in the original Ref. [40], where a positive ΔH_{seg} infers GB segregation). While both Ni and Zr are strong segregating elements in refractory metals, Ni is a well-known sintering aid for enabling solid-state activated sintering of W, Mo, and potentially other refractory metals (via forming liquid-like interfacial phases) [29, 32, 33], but Zr is not. Zr, being a more refractory alloying element than Ni, is less likely to promote sintering via forming liquid-like
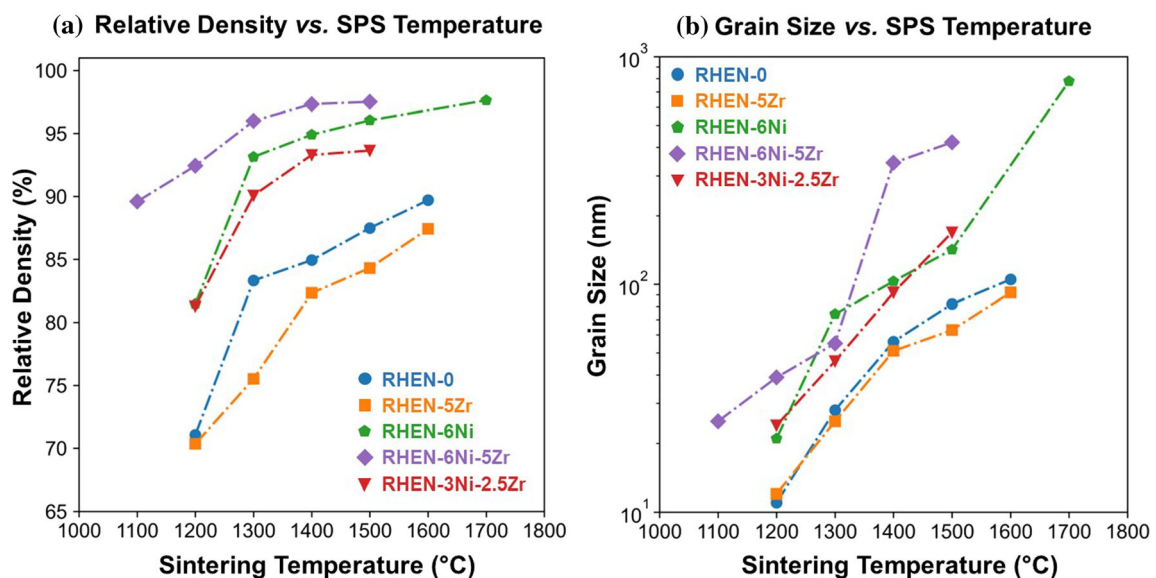

Figure 1 Measured **a** relative density and **b** grain size *vs.* SPS temperature curves for five series of REHNs after SPS. All specimens were hold isothermally at the sintering (SPS) temperatures for 5 min under 50 MPa of pressure.

interfacial phases. The melting temperature of Ni (T_m^{Ni} = 1455 °C) is 400 °C lower that of Zr (T_m^{Zr} = 1855 °C). The lowest eutectic temperatures in the five X-Ni binary alloys are > 200 °C lower than those of the corresponding X-Zr binary alloys (Table 1). Notably, the average solidus temperature for the five X-Ni binary alloys is 1608 °C, while that for the five X-Zr binary alloys is 2021 °C (Table 3). This is consistent with our observations that Ni addition promoted sintering in RHEA-6Ni, while Zr addition suppressed sintering in RHEA-5Zr (Fig. 1a). It is noted that we intentionally selected the Ni doping level (6%) to be higher than the solid solubility limits of all five X-Ni binary systems (Table 3); thus, we expect the formation of up to five secondary precipitation phases (according to the Gibbs phase rule) but all in small amounts. This can enable us to realize the hypothesized bulk high-entropy stabilization effects via Type II HEGBs, which will be discussed in Section 3.5.

On the one hand, the addition of 5% Zr slightly reduced both densification and grain growth, as shown by the blue (RHEN-0) *vs.* orange (RHEN-5Zr) curves in Figs. 1 and 2. On the other hand, the addition of 6% Ni significantly increased both densification and grain growth, as shown by the blue (RHEN-0) *vs.* green (RHEN-6Ni) curves in Figs. 1 and 2. For example, at SPS temperature of 1300 °C, addition of 6% Ni increased the relative density from ∼ 83.7% to ∼ 93.1% and ∼ 93.6%, respectively (for two independent specimens), and increased the mean grain size from ∼ 28 nm to ∼ 74 nm and ∼ 78 nm, respectively. Likewise, at SPS temperature of 1400 °C, addition of 6% Ni increased the relative density from ∼ 85.3% to ∼ 94.9% and ∼ 94.7, respectively (for two independent specimens), and increased the mean grain size from ∼ 56 nm to ∼ 103 nm and ∼ 109 nm,

respectively. In each case, two RHEN-6Ni specimens were prepared and sintered at nominally identical conditions, showing good repeatability of the densification and grain growth results (Fig. 5a, b and Supplementary Fig. S7 and S8).

We annealed the densest RHEN-5Zr-1600SPS. Similar to the undoped RHEN-0-1600SPS, isothermal annealing of RHEN-5Zr-1600SPS at 1100–1300 °C resulted in limited further densification and grain growth (Fig. 2 and Supplementary Table S2). For example, annealing at 1300 °C for 5 h increased the relative density of RHEN-5Zr moderately from ∼ 87.4% to ∼ 89.7%, with a moderate increase in the mean grain size from ∼ 92 nm to ∼ 117 nm.

We further annealed two series of Ni-doped specimens, RHEN-6Ni-1300SPS and RHEN-6Ni-1400SPS, isothermally at 1100–1300 °C for 5 h, which resulted in some further densification with limited grain growth (Fig. 3 and Supplementary Table S2). For example, annealing of RHEN-6Ni-1300SPS at 1300 °C for 5 h increased the relative density of RHEN-6Ni-1300SPS from ∼ 93.1% to ∼ 97.0%, with a moderate increase in the mean grain size from ∼ 74 nm to ∼ 133 nm, as shown in Fig. 5c and Supplementary Fig. S9. In addition, annealing of RHEN-6Ni-1400SPS (that was sintered at a higher SPS temperature of 1400 °C for 5 min to higher density and grain size) at 1300 °C for 5 h increased the relative density of RHEN-6Ni-1400SPS from ∼ 94.9% to ∼ 97.2%, with a smaller increase of the mean grain size from ∼ 103 nm to ∼ 124 nm, as shown in Fig. 5d and Supplementary Fig. S10. Interestingly, the final densities and grain sizes of the two series of specimens after isothermal annealing are similar, regardless of the initial SPS temperatures (1300 °C *vs.* 1400 °C). It appears that the isothermal annealing reduced the initial differences in these two series of RHEN-6Ni specimens (Fig. 5 and Supplementary Table S2).

Table 1 Summarized results of selected as-sintered RHENs, including compositions, SPS conditions, measured relative densities, and measured average grain sizes (± 1 standard deviation). Complete data for all 26 as-sintered RHENs made in this study are documented in Supplementary Table S1

Composition	SPS conditions		Relative density	Grain size
RHEN-6Ni (18.8Ti-18.8Nb-18.8Mo-18.8Ta-18.8W-6Ni)	1300 °C × 5 min	Specimen #1	93.1%	74 ± 19 nm
		Specimen #2	93.6%	78 ± 27 nm
	1400 °C × 5 min	Specimen #1	94.9%	103 ± 35 nm
		Specimen #2	94.7%	109 ± 40 nm
RHEA-6Ni-5Zr (17.8Ti-17.8Nb-17.8Mo-17.8Ta-17.8W-6Ni-5Zr)	1300 °C × 5 min		96.0%	55 ± 14 nm

(a) Relative Density vs. Annealing Temperature

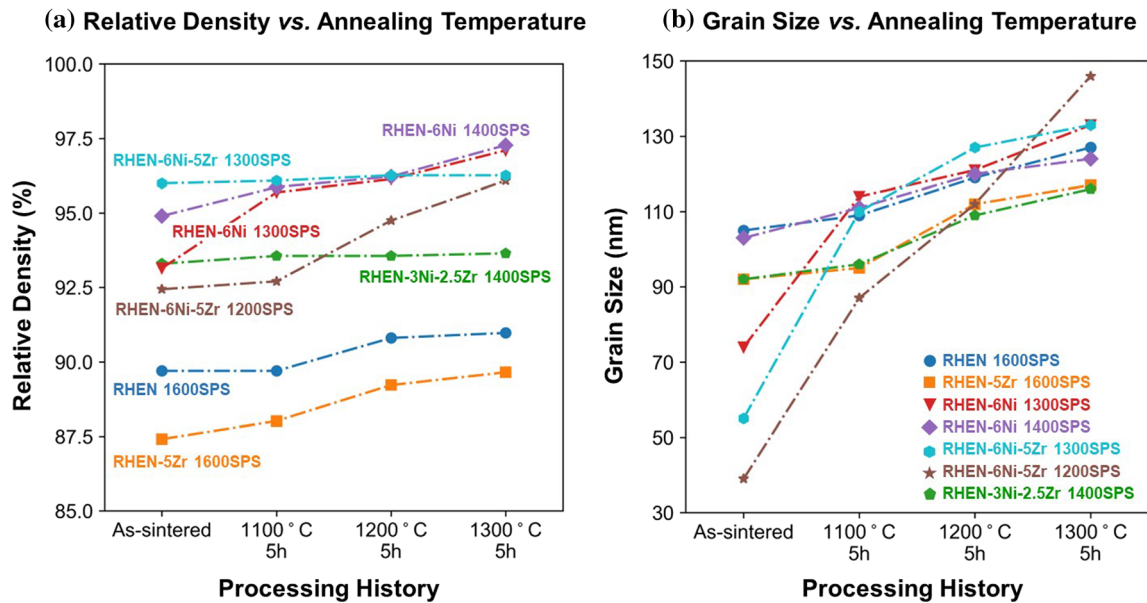**(b) Grain Size vs. Annealing Temperature**

Figure 3 Measured **a** relative density and **b** grain size *vs.* annealing temperature curves for the grain growth experiments, where seven series of RHENs were annealed at 1100 °C, 1200 °C, and 1300 °C, respectively, isothermally for 5 h. The corresponding data from the seven as-sintered RHENs before annealing are also shown as references.

Table 2 Summarized results of the three selected RHENs after annealing at 1300 °C for 5 h, including measured relative densities, average grain sizes, and Rockwell hardness (HRC)

Composition and processing history	Relative density (%)	SEM grain size (nm)	Hardness (HRC)
RHEN-6Ni 1300 °C × 5 min SPS + 1300 °C × 5 h Annealing	97.0	133 ± 28	64 ± 3
RHEA-6Ni 1400 °C × 5 min SPS + 1300 °C × 5 h Annealing	97.2	124 ± 10	65 ± 2
RHEA-6Ni-5Zr 1300 °C × 5 min SPS + 1300 °C × 5 h Annealing	96.3	133 ± 26	62 ± 4

More data for 28 annealed specimens in seven series of RHENs (*i.e.*, 21 annealed specimens, along with seven as-sintered RHENs before the annealing as the references) are documented in Supplementary Table S2

Notably, both $Ti_{18.8}Nb_{18.8}Mo_{18.8}Ta_{18.8}W_{18.8}Ni_6$ (RHEN-6Ni-1300SPS and RHEN-6Ni-1400SPS) specimens retained < 150 nm grain sizes with > 96% of the theoretical densities after five hours annealing at 1300 °C, representing some of the best high-temperature stability achieved.

Ni and Zr Co-doped RHENs

We further examined two Ni and Zr co-doped compositions, RHEN-6Ni-5Zr (doped with 6% Ni and 5% Zr) and RHEN-3Ni-2.5Zr (doped with 3% Ni and 2.5% Zr), both of which showed enhanced sintering in comparison with RHEN-0 (as shown by the purple/red *vs.* blue curves in Figs. 1a and 2).

In particular, RHEN-6Ni-5Zr showed further enhanced sintering in comparison with RHEN-6Ni,

particularly at low sintering temperatures (as shown by the purple *vs.* green curves in Fig. 1a). For RHEN-6Ni-5Zr, the grain growth was limited at SPS temperatures of 1100–1300 °C, but more substantial at SPS temperatures of 1400 °C and 1500 °C (Fig. 1b). The corresponding grain size *vs.* relative density curves for RHEN-6Ni-5Zr *vs.* RHEN-6Ni curves suggested that Zr co-doping enhanced densification via suppressing grain growth (as the curve for RHEN-6Ni-5Zr shifted towards the right in Fig. 2).

As an example, Fig. 6 shows the grain size distribution and SEM micrograph (with a view of a larger region in Supplementary Fig. S11 of RHEN-6Ni-5Zr sintered at 1300 °C, where we achieved a high relative density of ∼ 96% and a small mean grain size of ∼ 55 nm. This represents our best as-sintered

Table 3 Summary of relevant thermodynamic data of X-Ni and X-Zr (X = W, Mo, Ta, Nb, or Ti) binary alloys, including the solubilities at 1300 °C, the lowest eutectic temperatures, and solidus temperatures for given compositions (taken from binary phase diagrams shown in Supplementary Fig. S2 and Fig. S3 from ASM Alloy Phase Diagram Database^{TM}) and the segregation enthalpy ΔH_{seg} values calculated from a Miedema-based model by Murdoch and Schuh [40]

X	Solubility at 1300 °C (at%)		Lowest Eutectic temperature T_E (°C)		Solidus temperature T_S (°C)		Segregation enthalpy ΔH_{seg} (J/mol)	
	Ni in X	Zr in X	X-Ni	X-Zr	X-6Ni	X-5Zr	X-Ni	X-Zr
W	0.2	1.1	1500	1740	1500	2160	− 78276	− 58933
Mo	1.3	7	1312	1576	1360	1915	− 46901	− 47254
Ta	2.9	9.2	1366	1885	2700	2420	− 79917	− 30822
Nb	7	100	1158	1730	1278	1810	− 42351	− 19478
Ti	4.2	100	952	1554	1200	1800	− 24897	− 1280
Rule-of-mixture (RoM) average value:					1608	2021	− 54468	− 31553

Both Ni and Zr prefer to segregate at GBs in X (X = W, Mo, Ta, Nb, or Ti) in all ten binary systems. Here, we adopt a sign convention where a negative ΔH_{seg} value suggests positive GB segregation or GB enrichment [41] (differing from the sign convention used in the original Ref. [40] where a positive H_{seg} infers GB segregation)

nanocrystalline specimen with high density and small nanoscale grain size.

In addition, RHEN-3Ni-2.5Zr showed slightly less densification with similar grain growth in comparison with RHEN-6Ni (as shown by the red *vs.* green curves in Fig. 1), for which the corresponding grain size *vs.* relative density curves almost overlap one another (Fig. 2).

We annealed three selected series of Ni and Zr co-doped specimens, RHEN-6Ni-5Zr-1200SPS, RHEN-6Ni-5Zr-1300SPS, and RHEN-3Ni-2.5Zr-1400SPS (Fig. 2 and Supplementary Table S2). Both RHEN-6Ni-5Zr-1300SPS and RHEN-3Ni-2.5Zr-1400SPS exhibited moderate grain growth with virtually no further densification after isothermal annealing at 1100–1300 °C for 5 h. RHEN-6Ni-5Zr-1200SPS, which started with a lower relative density of ∼ 92.4% and a small grain size of ∼ 29 nm, exhibited more densification and grain growth, reaching a relative density of ∼ 96.1% and a mean grain size of ∼ 146 nm after annealing at 1300 °C for 5 h.

Figure 7 shows the grain size distribution and SEM micrograph (with a view of a larger region in Supplementary Fig. S12) of the RHEN-6Ni-5Zr-1300SPS specimen after annealing at 1300 °C for 5 h, showing ∼ 96.3% relative density and a mean grain size of ∼ 133 nm. Similarly, RHEN-6Ni-5Zr-1200SPS exhibited ∼ 96.1% relative density and ∼ 146 nm grain size after annealing at 1300 °C for 5 h. Akin to RHEN-6Ni, an interesting observation is that the final densities (∼ 96.1% *vs.* ∼ 96.3%) and grain sizes
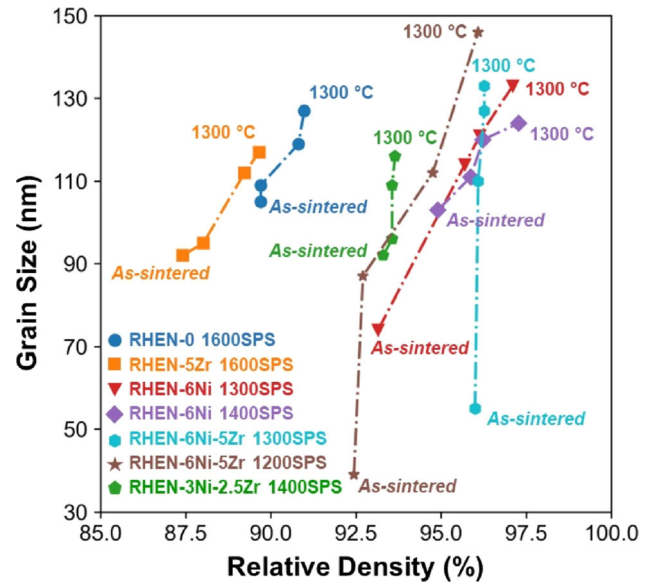

Figure 4 Grain size *vs.* relative density curves for seven series of as-sintered RHENs and specimens after annealing at 1100 °C, 1200 °C, and 1300 °C, respectively.

(∼ 146 nm *vs.* ∼ 133 nm) are similar after annealing at 1300 °C for 5 h, regardless of the initial SPS temperatures (1200 °C *vs.* 1300 °C) for these two RHEN-6Ni-5Zr specimens, where the isothermal annealing reduced the differences in initial relative densities (∼ 92.4% *vs.* ∼ 96.0%) and grain sizes (∼ 39 nm *vs.* ∼ 55 nm).
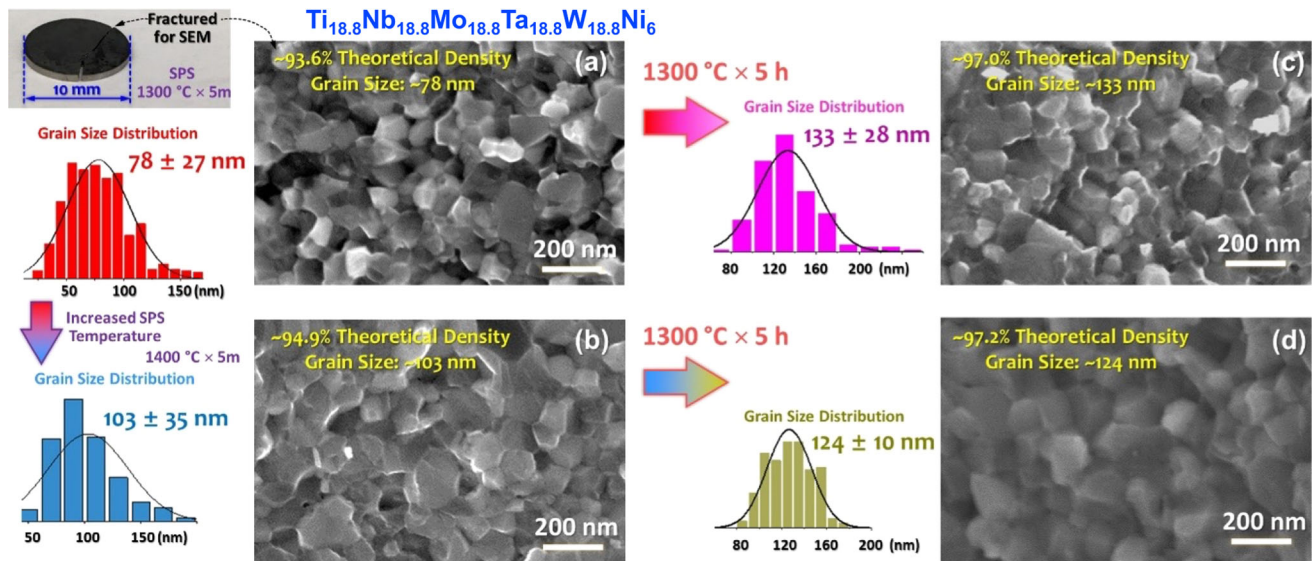
Figure 5 Grain size distributions and SEM micrographs of as-sintered RHEN-6Ni specimens sintered at **a** 1300 °C ($\sim$ 93.6%, $\sim$ 78 nm grain size) and **b** 1400 °C ($\sim$ 94.9% relative density, $\sim$ 103 nm grain size), respectively, and **c, d** after annealing at 1300 °C for 5 h with increased density (both to $\sim$ 97% relative densities) and limited grain growth (both < 150 nm in grain sizes). See Supplementary Figs. S7-S9 for additional specimens and views of larger regions of as-sintered and annealed RHEN-6Ni specimens.

The two $Ti_{17.8}Nb_{17.8}Mo_{17.8}Ta_{17.8}W_{17.8}Ni_6Zr_5$ specimens (RHEN-6Ni-5Zr-1200SPS and RHEN-6Ni-5Zr-1300SPS), in addition to two $Ti_{18.8}Nb_{18.8}Mo_{18.8}Ta_{18.8}W_{18.8}Ni_6$ specimens (RHEN-6Ni-1300SPS and RHEN-6Ni-1400SPS), all retained < 150 nm grain sizes with > 96% relative densities after five hours annealing at 1300 °C. Together they represent some of the highest temperature stability achieved for dense bulk nanoalloys and ultrafine-grained metals.

Discussion of possible mechanisms

The first main observation of this study is that addition of Ni (including Ni doping as well as Ni and Zr co-doping) can substantially improve the sintering of TiNbMoTaW-based RHENs. Prior studies showed that Ni promoted activated sintering of W and Mo via the formation of liquid-like interfacial phases at GBs (that can be explained as segregation-induced GB premelting [29, 32, 33]) and this mechanism were also found to be responsible for sub-eutectic activated sintering of ceramics like ZnO-Bi$_2$O$_3$ [42] and TiO$_2$-CuO [43]. In fact, it is well known that addition of Ni and other transition metals like Fe and Co can promote activated sintering of various refractory metals with proposed mechanisms based on segregation-

enhanced GB diffusion (in general) [29–32, 38, 39, 44, 45].

The stabilization of 2-D liquid-like interfacial phases below the bulk solidus temperatures is driven by the reduction of interfacial energies (that overcome the free-energy penalty to form nanometer-thick undercooled interfacial liquid films), which can be justified and predicted by thermodynamic models [33, 36, 37]. Interested readers are referred to the original modeling papers that first predicted the stabilization of liquid-like interfacial phases in binary [36] and multiple [46] refractory alloys, as well as a few further research [33] and review [26, 29, 37] papers that refined/elaborated the models and a most recent review on modeling more general GB phases (also called "complexions" [47]) and computing GB "phase" diagrams [48] for further elaboration of such 2-D interfacial phases, particularly the liquid-like complexions that can promote activated sintering.

Unfortunately, the nanoscale grain sizes in our RHENs made it infeasible to prepare good enough transmission electron microscopy (TEM) specimens to directly characterize the GBs. Nonetheless, it is likely that a mechanism similar to that which enables Ni activated sintering of W and Mo [29, 32, 33] is also responsible for Ni enhanced sintering of

TiNbMoTaW-based RHENs. While Zr segregation is likely too refractory to promote the formation of liquid-like GBs (as Zr is not a good activated sintering aid for Mo and W), co-doping RHENs with Ni and Zr can in principle enhance GB disordering via coupling effects (that were recently discovered in HEAs via atomistic simulations and machine learning [49]). Future investigations, *e.g.*, TEM characterization of coarse-grained alloys of the same compositions that are equilibrated and well-quenched from the high sintering temperatures as well as thermodynamic and atomistic modeling (that are non-trivial and beyond the scope of this study), may be conducted to further test the hypothesis and the underlying mechanism of Ni enhanced sintering of TiNbMo-TaW-based RHENs (that should occur via enhancing GB diffusion, regardless of the actual GB structures).

Activated sintering via forming liquid-like GBs (*i.e.*, via promoting GB diffusion) [29, 32, 33] would also likely promote grain growth. The second (perhaps even more interesting) observation of this study is that the addition of Ni, a well-known sintering aid for enabling activated sintering of W and Mo [29, 32, 33] (that are also expected to promote grain growth), in TiNbMoTaW-based RHENs can promote sintering without accelerating grain growth. Here, one possible mechanism is through the so-called "Type II HEGBs" (*i.e.*, HEGBs in HEAs, with a primary phase and multiple secondary phases as designed) following a hypothesis [27, 28] that adding a small but saturated amount of one strong segregating element in a HEA can provide improved high-temperature stability against grain growth, where the effect is more significant for a larger number of principal components in the bulk phase.
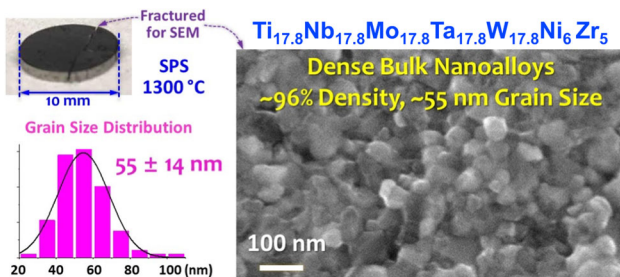

Figure 6 Grain size distribution and SEM micrograph of a RHEN-6Ni-5Zr specimen sintered at 1300 °C, showing a high relative density of ∼ 96% and a small mean grain size of ∼ 55 nm. SEM micrograph of a large region of this specimen is shown in Supplementary Fig. S11.

The key concept of Type II HEGBs [28] can be illustrated using a simplified model as follows (where we expand a more brief derivation originally given in a recent perspective article [28] and apply it to an idealized system to mimic our specific RHENs). Here, we adopt a multicomponent GB segregation model [26] generalized from the binary Wynblatt-Chatain model [41] to consider segregation in the two layers at the GB core of a general (large-angle) twist GB. To mimic TiNbMoTaW-Ni, let us consider a simplified, symmetric, $(N + 1)$-component ideal solution, where 1, 2, …, and N are (hypothetically) identical principal components (M_i) and $(N + 1)$ is a segregating component (S) and all binary i-$(N + 1)$ systems ($i = 1, 2, ..., N$) have identical thermodynamic parameters. We assume, for simplicity, the $(N + 1)^{\text{th}}$ component S is the only segregating component, so that a McLean-Langmuir type segregation equation applies:

$$\frac{X_{N+1}^{\text{GB}}}{X_{N+1}^{\text{bulk}}} = \frac{X_1^{\text{GB}}}{X_1^{\text{bulk}}} \exp\left(-\frac{\Delta g^{\text{seg.}}}{kT}\right) \approx \frac{X_1^{\text{GB}}}{X_1^{\text{bulk}}} \exp\left(-\frac{\Delta h^{\text{seg.}}}{kT}\right)$$

(1)

where X_i^{bulk} and X_i^{GB} are the bulk and GB compositions of the ith element, respectively, and $\Delta g^{\text{seg.}}$ ($\approx \Delta h^{\text{seg.}}$) is the free energy (enthalpy) change of the GB segregation of the $(N + 1)^{\text{th}}$ component. Here, we adopt the sign convention that $\Delta h^{\text{seg.}} < 0$ for positive GB segregation. We further assume:

$$\begin{cases} X_{N+1}^{\text{bulk}} << 1 \\ X_i^{\text{bulk}} = X_1^{\text{bulk}} = \dfrac{1 - X_{N+1}^{\text{bulk}}}{N+1} \quad \text{(for all } i = 1, 2, ... N) \\ N \cdot X_1^{\text{bulk}} + X_{N+1}^{\text{bulk}} = 1 \end{cases}$$

(2)

Then, we can derive from Gibbs adsorption theory (based on the lattice-type multicomponent GB segregation model [26, 41]) that GB energy is reduced with GB segregation, and further modified by the configurational entropy change at the GB, according to:

$$\begin{aligned} \gamma_{\text{GB}} &= \gamma_{\text{GB}}^{(0)} + 2n_{\text{PD}}\left[X_{N+1}^{\text{GB}}\Delta h^{\text{seg.}} + kT\sum_{i=1}^{N+1} X_i^{\text{GB}} \ln\left(\frac{X_i^{\text{GB}}}{X_i^{\text{bulk}}}\right)\right] \\ &= \gamma_{\text{GB}}^{(0)} + 2n_{\text{PD}}\left\{X_{N+1}^{\text{GB}}\left[\Delta h^{\text{seg.}} + kT \ln\left(\frac{X_{N+1}^{\text{GB}}}{X_{N+1}^{\text{bulk}}}\right)\right] + NkTX_1^{\text{GB}} \ln\left(\frac{X_1^{\text{GB}}}{X_1^{\text{bulk}}}\right)\right\} \end{aligned}$$

(3)

where $\gamma_{\text{GB}}^{(0)}$ is the reference GB energy of an undoped GB ($X_{N+1}^{\text{bulk}} = 0$), n_{PD} is the planar density of atoms

Ti$_{17.8}$Nb$_{17.8}$Mo$_{17.8}$Ta$_{17.8}$W$_{17.8}$Ni$_6$Zr$_5$ after annealing at 1300 °C x 5 h
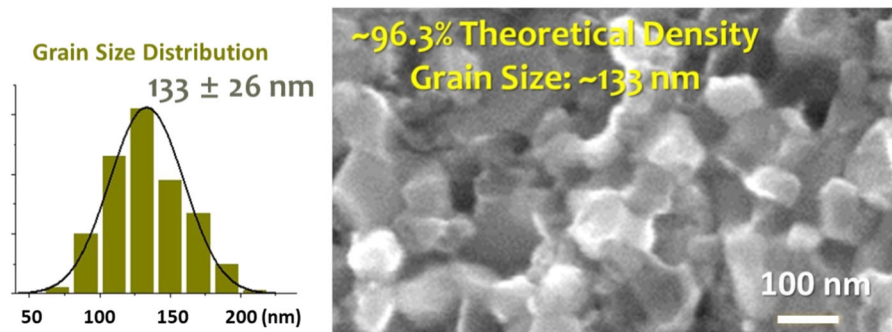

Figure 7 Grain size distribution and SEM micrograph of a RHEN-6Ni-5Zr-1300SPS specimen after annealing at 1300 °C for 5 h, showing ∼ 96.3% relative density and a mean grain size of ∼ 133 nm. SEM micrograph of a large region of this specimen is shown in Supplementary Fig. S12.

(noting there are two segregating layers at the twist GB considered here), k is the Boltzmann constant, and T is temperature. Plugging in Eq. (1) and taking Eq. (2), Eq. (3) can be simplified to:

$$
\begin{aligned}
\gamma_{\text{GB}} \approx &\gamma_{\text{GB}}^{(0)} + 2n_{\text{PD}}\left\{ X_{N+1}^{\text{GB}}\left[\Delta h^{seg.} + kT\ln\left(\frac{X_1^{\text{GB}}}{X_1^{\text{bulk}}}\right) - \Delta h^{seg.}\right]\right. \\
&\left. + NkTX_1^{\text{GB}}\ln\left(\frac{X_1^{\text{GB}}}{X_1^{\text{bulk}}}\right)\right\} \\
= &\gamma_{\text{GB}}^{(0)} + 2n_{\text{PD}}kT\left[X_N^{\text{GB}}\ln\left(\frac{X_1^{\text{GB}}}{X_1^{\text{bulk}}}\right) + NX_1^{\text{GB}}\ln\left(\frac{X_1^{\text{GB}}}{X_1^{\text{bulk}}}\right)\right] \\
= &\gamma_{\text{GB}}^{(0)} + 2nkT\ln\left(\frac{X_1^{\text{GB}}}{X_1^{\text{bulk}}}\right)
\end{aligned}
$$

$$(4)$$

We further assume that all binary solvus lines are pinned by stoichiometric $(M_i)_1(S)_1$ precipitation compounds (assumed 1:1 stoichiometry for simplicity) following:

$$X_{i,\text{binarysolvus}}^{\text{bulk}} \approx \exp(\Delta h^{\text{sol./ppt.}}/kT) \tag{5}$$

where $\Delta h^{\text{sol./ppt.}}$ (= $\Delta h_{i-(N+1)}^{\text{sol./ppt.}}$, assumed to be identical for all $i = 1, 2, ..., N$ for simplicity) < 0 is the enthalpy of dissolving an atom of the $(N + 1)^{\text{th}}$ element from the $(M_i)_1(S)_1$ precipitate in the binary i-$(N + 1)$ system. Thus, the maximum bulk solubility limit of the segregating $(N + 1)^{\text{th}}$ element in the $(N + 1)$-component system (obtained at $X_i^{\text{bulk}} = (1 - X_{N+1}^{\text{bulk}})/N$ for all $i = 1, 2, ..., N$) is given by:

$$X_{N+1}^{\text{bulk}} = N \cdot \exp\left(\frac{\Delta h^{\text{sol./ppt.}}}{kT}\right) \tag{6}$$

Here, we assume that our doping level of the $(N + 1)^{\text{th}}$ element S is greater than X_{N+1}^{bulk} so that the fraction of segregating element S in grains is on the maximum multicomponent solvus line at equilibrium (i.e., S-saturated grains in an equilibrium with N precipitated phases). Comparing Eq. (5) and Eq. (6) suggests that a bulk high-entropy effect that enhances the maximum solubility of the segregating $(N + 1)^{\text{th}}$ element S, which increases with the number of the principal components (N), which consequently enables Type II HEGBs to stabilize GB segregation at high temperatures and reduce GB energy with increasing N, as elaborated below. Combining Eq. (6) with Eq. (1) (and utilizing Eq. (2) and $N \cdot X_1^{\text{GB}} + X_{N+1}^{\text{GB}} = 1$), we can obtain:

$$X_{N+1}^{\text{GB}} = \frac{N\exp\left(-\frac{\Delta h_N^{\text{seg.-ppt.}}}{kT}\right)}{1 + N\exp\left(-\frac{\Delta h_N^{\text{seg.-ppt.}}}{kT}\right)} \tag{7}$$

where $\Delta h^{\text{seg.-ppt.}}$ ($\equiv \Delta h^{\text{seg.}} - \Delta h^{\text{sol./ppt.}}$) represents the enthalpy difference between the segregation and precipitation per atom. Equation (7) suggests that the amount of GB segregation increases with the number of the principal components (as $N\uparrow$) due to bulk high-entropy effects shown in Eq. (6) that increases the solid solubility of the segregating $(N + 1)^{\text{th}}$ element S.

Plugging Eq. (7) and $X_1^{\text{GB}} = (1 - X_{N+1}^{\text{GB}})/N$ into Eq. (4) and taking an approximation $X_1^{\text{bulk}} \approx 1/N$, we can derive an approximated analytical expression for an ideal solution at the dilute limit for a Type II HEGB in a HEA:

$$\gamma_{\mathrm{GB}} \approx \gamma_{\mathrm{GB}}^{(0)} - 2n_{\mathrm{PD}}kT\ln\left[1 + N\cdot\exp\left(-\frac{\Delta h_N^{\mathrm{seg.-ppt.}}}{kT}\right)\right]$$

$$(8)$$

An empirical relationship exists: $\Delta h_N^{\mathrm{seg.}} - \Delta h_N^{\mathrm{sol./ppt.}} \approx -(0.10 \pm 0.06)$ eV/atom $\approx -(10 \pm 6)$ kJ/mol [50], so that the term $\exp(-\Delta h_N^{\mathrm{seg.-ppt.}}/kT)$ is greater than 1 (~ 2.15 at 1300 °C, if we takes the medium value of 0.1 eV/atom). Equation (8) suggests more reduction in GB energy will reduce with increasing temperature ($\gamma_{GB}\downarrow$ as $T\uparrow$) and/or increasing the number of the principal components ($\gamma_{GB}\downarrow$ as $N\uparrow$).

Equation (8) suggests more reduction in GB energy with more principal elements ($\gamma_{GB}\downarrow$ as $N\uparrow$), which will provide thermodynamic stabilization (reducing the grain growth driving force). Equation (7) further suggests more GB segregation with more principal elements ($X_{N+1}^{\mathrm{GB}}\uparrow$ as $N\uparrow$), which will provide more kinetic stabilization via solute drag. Moreover, these bulk high-entropy effects in Type II HEGBs are more effective (to reduce GB energy γ_{GB} and increase GB segregation X_{N+1}^{GB}) at high temperatures (because $\exp(-\Delta h_N^{\mathrm{seg.-ppt.}}/kT)$ is a positive factor in both Eq. (7) and Eq. (8)). In other words, both the above hypothesized thermodynamic and kinetic stabilization mechanisms can be more effective with more principal elements (as $N\uparrow$) at high temperatures.

Consequently, this Type II HEGB effect can serve as one possible mechanism in stabilizing Ni-doped TiNbMoTaW RHENs against rapid grain growth (where $N = 5$ and Ni is the 6th segregating element, which can offer more stabilization effects than that in binary W–Ni and Mo-Ni alloys with $N = 1$, based on the above simplified model). We should note that the real RHENs are more complex, but the simplified and symmetric ideal solution model allows us to derive an analytical solution to illustrate a key mechanism to inhibit grain growth at high temperatures in HEAs with one strong segregating element via Type II HEGBs. This mechanism offers one possible explanation of our observation of exceptional high-temperature stability in Ni-doped RHENs ($\mathrm{Ti_{18.8}Nb_{18.8}Mo_{18.8}Ta_{18.8}W_{18.8}Ni_6}$ or RHEN-6Ni). The stabilization effects via Type II HEGBs can be further enhanced with co-doping (e.g., in RHEN-6Ni-5Zr and RHEN-3Ni-2.5Zr). We also recognize that secondary phase precipitates (from either the Ti–Nb–Mo–Ta–W–Ni–Zr systems or native oxides or impurities from ball milling) can also suppress grain growth via Zener pinning. Further investigations may quantify different stabilization mechanisms (albeit highly challenging given the complexity of real RHENs).

Again, it is important to emphasize that the real RHENs are much more complex (considering the interactions of all different components, multilayer adsorption [41, 51], and possible effects of GB chemical (adsorption) [51] and structural transitions [47, 48, 52], e.g., premelting like interfacial disordering that we discussed earlier for activated sintering [29, 37], all of which are not described in this simplified ideal model). In addition, we recognize that compositional inhomogeneity and secondary phase pinning can exist and affect grain growth in addition to the thermodynamic and kinetic effects of GB segregation (discussed here). Nonetheless, an approximated analytical solution from this simplified model can illustrate one of (but perhaps not the only) the possible mechanisms of high-temperature stability against rapid grain growth in Ni-doped RHENs (observed in this study) and potentially many other high-entropy nanoalloys (to be investigated in future studies).

Conclusions

In summary, this study has simultaneously achieved exceptional high-temperature stability and improved sinterability to fabricate a novel class of TiNbMoTaW-based refractory high-entropy nanoalloys (RHENs), with a primary BCC phase and multiple secondary phases (as designed to promote the formation of the so-called "Type II HEGBs", i.e., HEGBs in HEAs, with a primary high-entropy phase and multiple secondary phases). The effects of adding Ni and Zr in sintering and grain growth have been carefully examined. The fabricated bulk specimens (1 cm in diameter and ~ 3 mm in thickness) have achieved 93–96% relative densities with 50–100 nm grain sizes for three different compositions (albeit the anticipated existence of multiple secondary phases and possible compositional inhomogeneity). For example, a $\mathrm{Ti_{17.8}Nb_{17.8}Mo_{17.8}Ta_{17.8}W_{17.8}Ni_6Zr_5}$ fabricated by SPS at 1300 °C attained $\sim 96\%$ relative density with ~ 55 nm mean grain size. We further demonstrated that four different RHENs retained < 150 nm grain sizes with $> 96\%$ relative densities after five hours annealing at 1300 °C, which represent some of the highest temperature stability that has

been achieved for nanoalloys and ultrafine-grained metals.

Notably, the addition of Ni, a well-known sintering aid for activated sintering of refractory metals such as W and Mo (that would likely also promote grain growth through enhanced GB diffusion), in high-entropy TiNbMoTaW can promote sintering while maintaining high-temperature stability against rapid grain growth. This latter unusual observation can be explained by hypothesized effects of high-entropy grain boundaries (Type II HEGBs in HEAs) [28], for which we further elaborated the relevant theory with an idealized model [28] that gave a simplified analytical solution. We recognize other stabilization mechanisms, such as Zener pinning, can also be present in these complex RHENs.

Acknowledgements

Author contributions

MQ conducted most experiments and some data analysis (Data curation; Formal Analysis; Visualization). SS helped with data organization, characterization, analysis and drafted an initial manuscript (Data curation; Formal Analysis; Writing–original draft; Visualization). JL conceived the idea, supervised the study, and rewrote the manuscript (Conceptualization; Formal Analysis; Methodology; Supervision; Funding Acquisition; Writing–review & editing; Visualization).

Data availability

The data that support the findings of this study are available within the article and its supplementary material.

Declarations

Conflict of interest The authors declare no conflicts or competing interest.

Supplementary information See supplementary Tables S1-S2 and Figs. S1-S12 for detailed sintering and grain growth annealing experimental data, selected XRD patterns, additional SEM images of fractured surfaces before and after annealing, and relevant binary phase diagrams.

Supplementary Information: The online version contains supplementary material available at http s://doi.org/10.1007/s10853-023-08535-y.

References

[1] Rupert TJ, Schuh CA (2010) Sliding wear of nanocrystalline ni–w: structural evolution and the apparent breakdown of archard scaling. Acta Mater 58:4137–4148

[2] Liu Q, Wang G, Sui X, Liu Y, Li X, Yang J (2019) Microstructure and mechanical properties of ultra-fine grained monbtativ refractory high-entropy alloy fabricated by spark plasma sintering. J Mater Sci Technol 35:2600–2607

[3] Zou Y, Wheeler JM, Ma H, Okle P, Spolenak R (2017) Nanocrystalline high-entropy alloys: a new paradigm in high-temperature strength and stability. Nano Lett 17:1569–1574

[4] Koch CC, Scattergood RO, Darling KA, Semones JE (2008) Stabilization of nanocrystalline grain sizes by solute additions. J Mater Sci 43:7264–7272

[5] Koch CC (2007) Structural nanocrystalline materials: an overview. J Mater Sci 42:1403–1414

[6] Gleiter H (1989) Nanocrystalline materials. Prog Mater Sci 33:223–315. https://doi.org/10.1016/0079-6425(89)90001-7

[7] Günther B, Kumpmann A, Kunze HD (1992) Secondary recrystallization effects in nanostructured elemental metals. Scr Metall Mater 27:833–838. https://doi.org/10.1016/0956-716X(92)90401-Y

[8] Cahn JW (1962) The impurity drag effect in grain boundary motion. Acta Metall Mater 10:789–798

[9] Koju R, Darling K, Kecskes L, Mishin Y (2016) Zener pinning of grain boundaries and structural stability of immiscible alloys. Jom 68:1596–1604

[10] Weissmuller J (1994) Alloy thermodynamics in nanostructures. J Mater Res 9:4–7

[11] Weissmüller J (1993) Alloy effects in nanostructures. Nanostruct Mater 3:261–272

[12] Liu F, Kirchheim R (2004) Nano-scale grain growth inhibited by reducing grain boundary energy through solute segregation. J Cryst Growth 264:385–391

[13] Kirchheim R (2002) Grain coarsening inhibited by solute segregation. Acta Mater 50:413–419

[14] Kalidindi AR, Schuh CA (2017) Stability criteria for nanocrystalline alloys. Acta Mater 132:128–137

[15] Murdoch HA, Schuh CA (2013) Stability of binary nanocrystalline alloys against grain growth and phase separation. Acta Mater 61:2121–2132

[16] JR Trelewicz, CA Schuh (2009) Grain boundary segregation and thermodynamically stable binary nanocrystalline alloys. Phys Rev B 79:094112

[17] Chookajorn T, Murdoch HA, Schuh CA (2012) Design of stable nanocrystalline alloys. Science 337:951–954

[18] Kalidindi AR, Chookajorn T, Schuh CA (2015) Nanocrystalline materials at equilibrium: a thermodynamic review. JOM 67:2834–2843

[19] Jiao ZB, Schuh CA (2018) Nanocrystalline ag-w alloys lose stability upon solute desegregation from grain boundaries. Acta Mater 161:194–206

[20] Geoffrion LD, José-Yacaman M, Lehr A et al (2021) Substitutional–interstitial structural transition in cu–pt nano-alloys. Nanoscale Adv 3:3746–3751

[21] Haber JA, Buhro WE (1998) Kinetic instability of nanocrystalline aluminum prepared by chemical synthesis; facile room-temperature grain growth. J Am Chem Soc 120:10847–10855

[22] Darling KA, VanLeeuwen BK, Koch CC, Scattergood RO (2010) Thermal stability of nanocrystalline fe-zr alloys. Mater Sci Eng a-Struct Mater Prop Microstruct Process 527:3572–3580

[23] Haché MJ, Cheng C, Zou Y (2020) Nanostructured high-entropy materials. J Mater Res 35:1051–1075

[24] Koch CC (2017) Nanocrystalline high-entropy alloys. J Mater Res 32:3435–3444

[25] MR Zamani, H Mirzadeh, M Malekan, SC Cao, J-W Yeh (2022) Grain growth in high-entropy alloys (HEAs): a review. High Entropy Alloys Mater. https://doi.org/10.1007/s44210-022-00002-8

[26] Zhou N, Hu T, Luo J (2016) Grain boundary complexions in multicomponent alloys: challenges and opportunities. Curr Opin Solid State Mater Sci 20:268–277

[27] Zhou N, Hu T, Huang J, Luo J (2016) Stabilization of nanocrystalline alloys at high temperatures via utilizing high-entropy grain boundary complexions. Scripta Mater 124:160–163

[28] Luo J, Zhou N (2023) High-entropy grain boundaries. Commun Mater 4:7. https://doi.org/10.1038/s43246-023-00335-w

[29] Luo J (2012) Developing interfacial phase diagrams for applications in activated sintering and beyond: current status and future directions. J Am Ceram Soc 95:2358–2371

[30] Hayden HW, Brophy JH (1963) Activated sintering of tungsten with group viii elements. J Electrochem Soc 110:805–810. https://doi.org/10.1149/1.2425876

[31] German RM (1982) Activated sintering of refractory metals by transition metal additions. Rev Powder Metall Phys Ceram 2:9–43

[32] Gupta VK, Yoon DH, Meyer HM III, Luo J (2007) Thin intergranular films and solid-state activated sintering in nickel-doped tungsten. Acta Mater 55:3131–3142

[33] Shi X, Luo J (2011) Developing grain boundary diagrams as a materials science tool: a case study of nickel-doped molybdenum. Phys Rev B 84:014105

[34] Luo J, Gupta VK, Yoon DH, Meyer HM (2005) Segregation-induced grain boundary premelting in nickel-doped tungsten. Appl Phys Lett 87:231902. https://doi.org/10.1063/1.2138354

[35] Shi X, Luo J (2009) Grain boundary wetting and prewetting in Ni-doped Mo. Appl Phys Lett 94:251908. https://doi.org/10.1063/1.3155443

[36] Luo J, Shi X (2008) Grain boundary disordering in binary alloys. Appl Phys Lett 92:101901

[37] Luo J (2008) Liquid-like interface complexion: from activated sintering to grain boundary diagrams. Curr Opin Solid State Mater Sci 12:81–88

[38] Panichkina VV et al (1967) Activated sintering tungsten and molybdenum powders. Soviet Powder Metall Phys Ceram 6:558–560

[39] JH Brophy, LA Shepard, J Wulff (1961) Leszynski W (ed) Powder Metallurgy Interscience,

[40] Murdoch HA, Schuh CA (2013) Estimation of grain boundary segregation enthalpy and its role in

stable nanocrystalline alloy design. J Mater Res 28:2154–2163

[41] Wynblatt P, Chatain D (2006) Anisotropy of segregation at grain boundaries and surfaces. Metall Mater Trans a-Phys Metall Mater Sci 37A:2595–2620

[42] Luo J, Wang H, Chiang Y-M (1999) Origin of solid state activated sintering in bi2o3-doped zno. J Am Ceram Soc 82:916

[43] Nie J, Chan JM, Qin M, Zhou N, Luo J (2017) Liquid-like grain boundary complexion and sub-eutectic activated sintering in cuo-doped tio 2. Acta Mater 130:329–338

[44] Flether G, James MR, Moon JR (1971) The nickel activated sintering of tungsten. Scr Metall 5:105–107

[45] Lee DN, Ahn SH (1979) Nickel activated model sintering of tungsten. Sci Sinter 11:43–54

[46] Zhou NX, Luo J (2015) Developing grain boundary diagrams for multicomponent alloys. Acta Mater 91:202–206

[47] Cantwell PR, Tang M, Dillon SJ, Luo J, Rohrer GS, Harmer MP (2014) Grain boundary complexions. Acta Mater 62:1–48

[48] Luo J (2023) Computing grain boundary "phase" diagrams. Interdiscip Mater 2:137–160

[49] Hu C, Luo J (2022) Data-driven prediction of grain boundary segregation and disordering in high-entropy alloys in a 5d space. Mater Horiz 9:1023–1035

[50] Seah MP (1980) Grain boundary segregation. J Phys F: Met Phys 10:1043–1064

[51] Zhou N, Hu C, Luo J (2021) Grain boundary segregation transitions and critical phenomena in binary regular solutions: a systematics of complexion diagrams with universal characters. Acta Mater 221:117375. https://doi.org/10.1016/j.actamat.2021.117375

[52] Cantwell PR, Frolov T, Rupert TJ et al (2020) Grain boundary complexion transitions. Ann Rev Mater Res 50:465–492